The dislocation mechanism of stress corrosion embrittlement in Ti-6Al-2Sn-4Zr-6Mo

TP Chapman[1], VA Vorontsov[1], A Sankaran[1], D Rugg[2], TC Lindley[1], D Dye[1]

[1] *Department of Materials, Royal School of Mines, Imperial College London, Prince Consort Road, London, SW7 2BP, UK*

[2] *Rolls-Royce plc., Elton Road, Derby, DE24 8BJ, UK*

Abstract

An observation of the dislocation mechanisms operating below a naturally initiated hot salt stress corrosion crack is presented, suggesting how hydrogen may contribute to embrittlement. The observations are consistent with the hydrogen enhanced localised plasticity mechanism. Dislocation activity has been investigated through post-mortem examination of thin foils prepared by focussed ion beam milling, lifted directly from the fracture surface. The results are in agreement with existing studies, suggesting that hydrogen enhances dislocation motion. It is found that the presence of hydrogen in (solid) solution results in dislocation motion on slip systems that would not normally be expected to be active. A rationale is presented regarding the interplay of dislocation density and the hydrogen diffusion length.

Key words: Titanium alloys, TEM, Dislocation, Fatigue, Hydrogen embrittlement

1. Introduction

Titanium alloys are widely used in aerospace applications, as they offer high usable specific fatigue strengths at temperatures up to $\sim 550\,^{\circ}\mathrm{C}$ [1, 2, 3, 4]. In the vast majority of cases titanium alloys are highly corrosion resistant, which has also lead to their use in petrochemical and chemical process industries. However, under certain environmental conditions, the adherent and protec-

tive TiO_2 scale is broken down, exposing the underlying metal to attack [5]. The unwelcome discovery of this problem in the 1960s lead to extensive research [6, 7, 8, 9, 10, 11, 12], which has continued to the present day [13, 14]. In 1972, Blackburn et al (in [15]), found titanium to be susceptible to stress corrosion cracking (SCC) under a variety of aggressive media, including nitric acid, nitrogen tetroxide and molten salts. Particular consideration was given to the effect of NaCl at temperatures above $\sim 300\,^{\circ}\mathrm{C}$ [9]. Titanium was found to be highly vulnerable to SCC in the presence of aqueous sodium chloride, which was of particular concern in aerospace service applications.

Soon after the vulnerability of Ti alloys to SCC was discovered, hydrogen began to be implicated in the process. Some studies suggested a mechanism involving the production of $HCl_{(g)}$, and a consequent dissociation of the hydrogen chloride into chloride ions and dissolved hydrogen in solution [8, 9, 11]. Hydrogen is known be detrimental to the mechanical properties of Ti alloys, including a loss in ductility and enhanced crack growth rates in fatigue [16]. Several mechanisms for this have been offered. Hydrogen has a terminal solubility as high as 50 at.% in the bcc β-phase, compared to ~ 7 at.% in the hcp α-phase. In hydride forming near-α alloys, this might lead to formation and cleavage of brittle hydride precipitates. However, the operative mechanism in non-hydride forming systems is still under debate. Many authors hypothesise that interstitial hydrogen will segregate to α/β interfaces [17], where it might weaken the cohesive strength (hydrogen-enhanced decohesion, HEDE), resulting in intergranular separation of the interfaces [18, 19, 10]. Shih et al. [20], consider there to be minimal experimental evidence supporting this interface decohesion theory. Instead, they propose an alternative mechanism, supporting previous work by Beachem, where hydrogen enhanced localised plasticity (HELP) in the vicinity of the crack tip is suggested [21, 22]. Another postulated mechanism is adsorption-induced dislocation emission (AIDE), where hydrogen adsorbed within a few atomic distances of the crack tip results in dislocation emission from the crack tip [23, 24, 25]. The difference compared to the HELP mechanism chiefly concerns whether hydrogen diffusion into the bulk is implied.

Not only is hydrogen more soluble in the beta phase, it is also able to diffuse much more rapidly in the body centred cubic (bcc) β structure than in the close-packed α phase [26]. In two-phase α/β titanium alloys, a continuous beta phase is then supposed to provide a "short circuit path" for hydrogen transport [27, 18, 19]. Pao and O'Neal [28] suggested that hydrogen diffusion in the continuous beta ligaments of Ti-6242S could be the rate controlling process for hydrogen enhanced fatigue crack growth. Thus, lamellar microstructures with continuous β-phase could be more vulnerable to hydrogen effects.

The α/β alloy, Ti-6Al-2Sn-4Zr-6Mo (Ti-6246 - wt.%) offers an increase in operating temperature of up to 150°C when compared to the workhorse alloy, Ti-6Al-4V (Ti-64 - wt.%), predominantly due to its high strength owing to the formation of fine-scale secondary α. Therefore Ti-6246 is now commonly used in applications up to 500 °C, whereas Ti-64 is restricted to cooler locations in the jet engine.

In a companion study [29], we examined the formation mechanism of a blue-coloured fatigue crack initiation feature observed at the origin of several fracture surfaces from elevated temperature spinning rig and test specimens, some of which were found to have reduced fatigue lives. Evidence of chlorine within the "blue spot" was observed by scanning transmission electron microscopy based energy dispersive X-ray analysis (STEM-EDX). The blue spot was also found to possess a thick ($\sim 200\,\mathrm{nm}$) TiO_2 oxide scale. Further evidence for $^{35}Cl^-$, $^{23}Na^+$ and $^{16}O^-$ was found using focussed ion beam-secondary ion mass spectrometry (FIB-SIMS). A hot salt stress corrosion cracking (HSSCC) mechanism was proposed as an explanation for the apparent change in fracture mode seen at the fatigue crack origin.

In summary, the corrosion mechanism was held to operate as follows. First, the (NaCl) salt deposit reacts with atmospheric moisture and the oxide to produce $HCl_{(g)}$ and sodium titanate. This reaction disrupts the oxide scale, allowing the HCl to then react with the exposed metal, forming titanium alloy chlorides and hydrogen. The volatile alloy chlorides can then escape from the corrosion crack to react with moisture, precipitating a TiO_2 corrosion product

and re-forming HCl. The hydrogen produced can then diffuse into the metal at the crack tip, where it remains because hydrogen concentrates at regions of high stress triaxiality [12, 30]. Therefore, the extent of embrittlement is controlled by a competing reaction of hydrogen charging vs. hydrogen diffusion, with hydrogen assisting the cracking process. Eventually, and with a finite supply of salt, the Cl supply will become exhausted due to losses from the system, resulting in a decrease in hydrogen charging. Therefore beyond a certain crack length, a transition from HSSCC to conventional fatigue crack propagation was observed.

Therefore it remains to explain how the hydrogen embrittling mechanism operated in practice, through HELP or otherwise, in this naturally initiated cracking process. Previously, Robertson and co-workers have used hydrogen-containing *in situ* straining cells in the TEM to examine the effect of hydrogen on dislocation activity [20, 31, 32, 33]. These studies suggested that hydrogen enhances dislocation motion by locally reducing the stress required to cause motion and/or increasing the velocity. Shih et al. showed that by adding and removing hydrogen from the environment cell, they could control slip activity at the crack tip [20]. Hydrogen shielding was proposed as a rationale for this enhanced mobility [31, 32, 33].

In this work we examine the dislocations underlying the "blue spot" corrosion fatigue crack origin, compared to the low cycle fatigue situation, to determine if a change in dislocation mechanisms is observable. This will be of particular utility for the investigation of failures where hydrogen-enhanced cracking is suspected to be involved.

2. Material and Experimental Procedures

[Figure 1 about here.]

The Ti-6246 material used during this study was provided by Rolls-Royce plc., and was tested at the Mechanical Testing Operations Center (MTOC), Rolls-Royce Deutschland. Two specimens were examined ("blue spot" specimen U7-086 [29] and "datum" specimen LCF127) which were tested at 450 °C with

a maximum stress (σ_{max}) of 600 MPa (U7-086) and 640 MPa (LCF127) and an R ratio of 0.1. The material was processed with a final heat treatment in the β phase field followed by ageing in the $\alpha + \beta$ phase field, to produce the lamellar microstructure shown in Figure 1. The microstructure consisted of coarse, high aspect ratio primary α laths, and fine secondary α laths residing within a retained β matrix. Fully lamellar microstructures are used to maximise fracture toughness [5], with elevated strength provided by the fine secondary alpha phase.

The spatial and crystallographic orientation of facetted fracture features at the hydrogen embrittled origin were determined using quantitative tilt fractography (QTF) and electron backscattered diffraction (EBSD). A Zeiss Auriga field emission gun - secondary electron microscope (FEG-SEM), fitted with an Oxford Instruments EBSD detector, was used. By identifying the spatial orientation of the fracture features using QTF [34, 35, 36] it was possible to index Kikuchi diffraction patterns obtained directly from the fracture surface. Two facets within the hydrogen embrittled initiation site were analysed, Figure 2.

[Figure 2 about here.]

[Figure 3 about here.]

In situ FIB lift out was used for the preparation of thin foils from the "blue spot" origin in U7-086, Figure 2, from the crack initiation site in LCCF127 and from the region of fatigue crack growth in U7-086, 600 µm from the origin. FIB milling was carefully performed so as to minimise the surface damage due to irradiation by the Ga^+ beam [37, 38], commonly attributed to Ga^+ ion implantation, which can, in some cases, affect defect structures. Initially, a sample was produced from as-received material that had not undergone further deformation since forging, using a dual beam FEI Helios NanoLab 600. Approximately 2 µm of platinum was deposited onto the region of interest to protect the surface from the 30 kV primary Ga^+ beam. After lift-out, the sample was thinned down to $\sim$ 180 nm. The final thinning stage involved low current (28 pA), low

energy (2 keV) polishing, to remove ∼20 nm of material from the front and back of the sample. A comparison sample was prepared from the same as-received material using conventional electropolishing with a solution of 3% perchloric acid and 40% butan-1-ol in 57% methanol at 24 V and -40 °C. Both samples provided consistent results in the TEM, see Appendix. All site-specific samples were then lifted directly from the fracture surface using the same FIB lift-out procedure. The optimal sample thickness was found to be ~ 180 nm. This was thick enough to observe clear Kikuchi lines, while achieving adequate imaging conditions. For consistency, all analysis was undertaken on primary alpha laths, as shown in Figure 3.

Dislocations within grains connected to the fracture surface were examined using a combination of invisibility contrast conditions, alongside trace analysis, using a 200 keV JEOL 2000FX TEM. The grains of interest were imaged with $\mathbf{g} = \{0002\}$, $\{0\bar{1}11\}$ and $\{0\bar{1}1\bar{1}\}$, as well as $\{10\bar{1}0\}$, $\{\bar{2}110\}$ and $\{0\bar{1}12\}$ if possible, where $\mathbf{g}$ is the reciprocal lattice vector. The Burgers vectors, $\mathbf{b}$, of screw dislocations were then differentiated by calculating invisibility contrast values as the scalar product of the reciprocal lattice vector and possible Burgers vectors ($\mathbf{g} \cdot \mathbf{b}$). Edge discloations were analysed by considering contrast values calculated by $\mathbf{g} \cdot (\mathbf{b} \times \mathbf{l})$, where $\mathbf{l}$ is the line vector. By incorporating trace analysis, it was possible (in some cases) to determine the active slip system. Considering the orientation of the grain with respect to the fatigue loading axis, comparisons with favourable slip systems according to Schmid factor calculations could also be made.

3. Results

3.1. Facet orientation

The spatial and crystallographic orientation of two facets residing within the hydrogen embrittled initiation site were analysed using QTF/EBSD. It was found that facet 1 and facet 2 were spatially orientated such that each facet normal was $<10\,^\circ$ away from the tensile loading axis. By accounting for the

angular deviation of the facet normal away from the loading direction in the EBSD, the crystallographic orientation of each facet could then be acquired. This made it possible to index directly from the fracture surface without the need for prior sectioning and surface preparation. With reference to the [0001] pole figures, demonstrated in Figure 4, it can be seen that both facet normals lie close to the [0001] direction. In fact, the facet normals are measured to be orientated $\sim 14^\circ$ away from the [0001] direction, indicating that the plane of the facet, and thus fracture plane, coincides with either the $\{10\bar{1}7\}$ or $\{10\bar{1}8\}$ planes, inclined at 15° and 13° away from the basal plane respectively. Both the $\{10\bar{1}7\}$ and $\{10\bar{1}8\}$ planes are known to be common hydrogen habit planes [39], indicating that the fracture mechanism is likely to have been modified by the presence of hydrogen. It should be noted that the three low intensity spots in Figure 4(b) have arisen from indexing of an adjacent, and differently orientated grain.

[Figure 4 about here.]

3.2. Dislocation contrast analysis

Three FIB prepared foils, containing grains 1-4, were lifted directly from the low cycle fatigue fracture surface that suffered HSSCC (sample U7-086). Grains 1, 2 and 3 are associated with an area embrittled by hydrogen, near the fatigue crack origin; Figure 2(LOM) demonstrates the location of foil within the hydrogen embrittled origin. Grain 4 resided within a foil that was milled from an area of fatigue crack propagation, approximately 600 µm from the origin. Finally, grain 5 was observed within a foil that was milled from the origin of a different LCF specimen, that had not undergone hydrogen embrittlement (sample LCF 127). To have the best chance of observing dislocation mechanisms associated with the fracture process, it was deemed important to analyse grains connected to the fracture surface, i.e. not subsurface; Figure 3 shows the positions of the analysed grains with respect to the fracture surface.

[Table 1 about here.]

3.2.1. Hydrogen assisted fatigue cracking

Grain 1's {0002} plane normal was found to be $\sim 70^\circ$ to the tensile-fatigue loading axis. Figure 5(a) shows bright field (BF) TEM micrographs, imaged with several diffraction conditions. For $\mathbf{g}_{0002}$, an array of linear dislocation segments were observed across the width of the primary alpha grain, $\sim$ 700 nm to 1.5 µm beneath the fracture surface. The dislocations appear to be orientated almost parallel to the (0002) trace, obtained from the $\langle 1\bar{2}10\rangle$ selected area diffraction pattern (SADP). Referring to the 4-index *hcp* coordinate system, it can be said that the beam direction vector ($\mathbf{B}$) lies in the basal plane of the crystal and is parallel to two of the $\langle a\rangle$ type Burgers vectors. Any dislocations residing in the basal plane, and imaged under these conditions edge-on, would appear as straight line segments, parallel to the (0002) trace. Slight misorientation between the trace and the dislocation segment is likely to result from the small rotation of the SADP (from which the trace is obtained) when the sample is tilted away from the pole to reach the required $\mathbf{g}$ vector. From trace analysis, it is therefore implied that the array of dislocations in Figure 5 ($\mathbf{g}_{0002}$) has resulted from slip on the basal plane.

Basal glide has frequently been observed in α titanium, but this occurs almost exclusively with $\langle 11\bar{2}0\rangle$ type Burgers vectors. Under $\mathbf{g}_{0002}$ diffraction conditions, as in Figure 5 (upper), all screw dislocations with $\langle a\rangle$ type $\langle 11\bar{2}0\rangle$ Burgers vectors should have zero contrast, and thus be invisible, which is not the case here. It then became necessary to evaluate the edge component also, incorporating the $\mathbf{g}\cdot(\mathbf{b}\times\mathbf{l})$ criterion. Introducing a perpendicular line vector, with indices $\langle 1\bar{1}00\rangle$, demonstrates positive contrast for edge dislocations gliding on (0002) planes, when imaged with $\mathbf{g}_{0002}$. However, for all the $\{1\bar{1}00\}$ glide planes, there is zero contrast for dislocations with $\langle 11\bar{2}0\rangle$ Burgers vectors. This finding eliminates the possibility of prismatic slip in this case. Hence, considering the contrast criteria and the minimal misorientation between the (0002) trace and the dislocation segments, one possibility is that the linear dislocations segments in Figure 5 ($\mathbf{g}_{0002}$) are associated with $\langle 11\bar{2}0\rangle\{0001\}$ type slip systems,

and have edge character.

[Figure 5 about here.]

[Table 2 about here.]

An alternative hypothesis could be that these dislocations are of $\langle c+a \rangle$ type. Both edge and screw character $\langle c+a \rangle$ dislocations have contrast at imaging conditions of $\mathbf{g}_{0002}$. Glide in the direction of such Burgers vectors is restricted to the pyramidal planes $\{10\bar{1}0\}$ and $\{11\bar{2}2\}$. Under imaging conditions of $\mathbf{B} \sim \langle 2\bar{1}\bar{1}0 \rangle$, these inclined planes would be viewed at a small angle to the face of the plane, rather than edge on, and hence may not be expected to appear as straight lines as they do for conditions of $\mathbf{g}_{0002}$. However, $\langle c+a \rangle$ dislocations have an inherently higher elastic energy compared to the $\langle a \rangle$ type. Hence it is reasonable that such dislocations could exist as straight lines to minimise this energy, rather than the bowed out segments and loops that may be observed from $\langle a \rangle$ type line defects.

The same area was viewed at alternative diffraction conditions of $\mathbf{g}_{0\bar{1}1\bar{1}}$ and $\mathbf{g}_{0\bar{1}11}$ in an attempt to determine the active dislocation type. Contrast of the original linear dislocation array, as seen for $\mathbf{g}_{0002}$, remains for both $\mathbf{g}_{0\bar{1}1\bar{1}}$ and $\mathbf{g}_{0\bar{1}11}$, in varying intensity. This observation essentially excludes edge $\langle c+a \rangle$ dislocations gliding on first order pyramidal planes, since the invisibility criterion suggests zero contrast for either $\mathbf{g}_{0\bar{1}1\bar{1}}$ and $\mathbf{g}_{0\bar{1}11}$, in most cases. Table 2 provides details of the invisibility criterion for a number of $\mathbf{g}$ vectors. Furthermore, the elastic energy of a dislocation is proportional to the magnitude of the Burgers vector, with the $\langle c+a \rangle$ energy almost twice that of the $\langle a \rangle$ type Burgers vector. Finally edge $\langle a \rangle$ show zero contrast at $\mathbf{g}_{0002}$ for prismatic planes and at $\mathbf{g}_{0\bar{1}11}$ for first order pyramidal planes. Hence, it is tentatively suggested that the linear dislocation arrays observed for grain 1 in Figure 5 are associated with edge dislocations undergoing basal slip in the direction of $\langle 11\bar{2}0 \rangle$ type Burgers vectors.

Closer investigation of Figure 5(b) reveals a number of shorter dislocation segments orientated $\sim 120^\circ$ to the (0002) trace. Both the first and second

order pyramidal slip planes are inclined $\sim 120^\circ$ to the basal plane. First order $\{1\bar{1}01\}$ planes are able to slip along either $\langle c+a \rangle$ type $\langle 11\bar{2}3 \rangle$ or $\langle a \rangle$ type $\langle 11\bar{2}0 \rangle$ Burgers vectors, whereas second order $\{\bar{1}\bar{1}22\}$ planes are restricted to glide in the $\langle c+a \rangle$ direction only. Under certain diffraction conditions, the short angled segments move out of contrast whilst those longer sections, parallel to the (0002) trace, remain in contrast. It is hence implied that the short, orientated segments observed have a different Burgers vector to the remainder of the linear array.

The observations made from analysis of grain 2 are consistent with those from grain 1, which has the same crystal orientation. The uppermost image in Figure 6 shows the full length of the primary alpha lath, identified as grain 2. In this case, the straight dislocation segments are observed up to 3 µm beneath the fracture surface. Beyond this depth, similar dislocations are not observed. In fact, beyond 3 µm below the surface, only a small group of differently orientated dislocations can be identified at the very tip of the primary alpha lath. Presumably, these have arisen as a result of grain 2 growth during processing, and the consequent collision with another primary alpha lath; refer to Figure 3, hydrogen origin foil 1. These observations again suggest that these dislocation structures are restricted to material only a few microns sub-surface of the growing crack. Observations based on trace analysis and invisibility contrast suggest that, like grain 1, the linear dislocation segments spanning across the lath have edge character, and have arisen from $\langle 11\bar{2}0 \rangle \{0001\}$ type slip. Imaging under $\mathbf{g}_{0\bar{1}1\bar{1}}$ repeats these findings; Figure 6. With reference to the high magnification micrograph for $\mathbf{g}_{0002}$ given in Figure 6, the short, inclined dislocation segments first observed in grain 1, are indicated again in grain 2. In this instance, at least three individual linear dislocations can be resolved, with each inclining away from the (0002) trace at angles between $\sim 105 - 120^\circ$. A collection of non-linear dislocations can also be identified directly beneath the fracture surface of grain 2 for conditions of $\mathbf{g}_{0002}$; see low magnification image. These looping dislocations appear to have been emitted from the 200 nm thick oxide layer, that covers the hydrogen embrittled origin. It is, however, unclear whether these dislocations were present prior to thin foil preparation, and may

in fact be a consequence of the platinum deposition process. For this reason they will not be discussed in more detail.

[Figure 6 about here.]

[Figure 7 about here.]

The c-axis of grain 3 is inclined at $\sim 25\,^\circ$ to the fatigue loading axis, compared to a $70\,^\circ$ inclination for both grains 1 and 2. The contrast observed for grain 3 at each diffraction condition can be described by the invisibility criterion given for edge $\langle a \rangle \frac{1}{3}[\bar{1}\bar{1}20]$ and edge $\langle c+a \rangle \frac{1}{3}[1\bar{2}13]$ dislocations, gliding on $(\bar{1}101)$ planes in both cases; as given in Table 2. Since dislocation contrast is observed for $\mathbf{g}_{0002}$ and $\mathbf{g}_{10\bar{1}0}$, both screw $\langle a \rangle$ and $\langle c+a \rangle$ dislocations can be excluded. Similarly, strong contrast for $\mathbf{g}_{\bar{2}110}$ and $\mathbf{g}_{0002}$ eliminates edge $\langle a \rangle \frac{1}{3}[\bar{1}\bar{1}20]$ dislocations gliding on basal and prismatic planes respectively; refer to Figure 7. It is therefore suggested that dislocations are moving on the first order pyramidal $(\bar{1}101)$ plane. Considering the increased elastic energy of $\langle c+a \rangle$ dislocations compared to the $\langle a \rangle$, it is not unreasonable to expect the dislocations to be $\langle a \rangle$ type in nature.

Figure 7 presents increased magnification micrographs of a bright field image for $\mathbf{g}_{0\bar{1}\bar{1}2}$. Two rows of parallel dislocation arrays are seen to give contrast at these imaging conditions, as discussed above. Consistent with findings from grains 1 and 2, the dislocations only reside immediately beneath the fracture surface, up to $\sim 1.5\,\mu$m sub-surface. Considering the FIB foil in 3D, but noting its transparency, it is likely that the discontinuous appearance of the dislocation segments is an effect of the position and orientation of the dislocations within the foil. Moreover, because the dislocations do not lie in the plane of the foil, and thus are restricted to the foil thickness, they appear in short segments where they "run out" the front and back planes of the foil. The two rows observed here, are considered to be dislocations residing on parallel and adjacent sets of planes.

[Figure 8 about here.]

3.2.2. Fatigue crack propagation

Grain 4 was located within a thin foil that was lifted from the U7-086 sample fracture surface at a crack length of $\sim 600\,\mu m$. As the crack exceeded $\sim 100\,\mu m$ in length, there was an observed transition in the cracking mechanism from HSSCC near the origin, to a low cycle fatigue crack propagation. Grain 4 has therefore not experienced any effect of solute hydrogen. Since grains 3 and 4 have similar crystallographic orientations ($\{0002\}$ normal $\sim 25^\circ$ vs. $\sim 30^\circ$ from the loading axis), direct comparisons can be made between them. Figure 8 provides BF diffraction contrast images taken with diffraction conditions of $\mathbf{g}_{0002}$. A high dislocation density is seen to extend down the length of the primary alpha laths. This is in stark contrast to observations from hydrogen embrittled grains. For grains 1-3, a low density of individual dislocation arrays were observed, and appeared to be restricted to the first few microns, directly beneath the fracture surface. The low magnification image given in Figure 8 has been included to demonstrate these differences. Although not included here, images showing similarly high dislocation densities were also obtained for several other diffraction conditions. A high dislocation density visible for several $\mathbf{g}$ vectors indicates that a large number of dislocations were active during the deformation process. As the dislocations move they will interact with each other, and likely entangle as they intersect.

Unlike the hydrogen embrittled grains 1-3, where a single slip system could be identified, it is likely that dislocations with different Burgers vectors and gliding on various planes, has led to the high densities observed in grain 4 and the adjacent laths. However, detailed examination of Figure 8 reveals that the bands of the most highly dense dislocation entanglements appear to be almost parallel to the (0002) trace. By observing the highest density bands in neighbouring primary alpha grains, it is suggested that these dislocations may have been transmitted across the secondary alpha/beta matrix ligaments, and continue into the adjacent primary alpha lath.

3.2.3. Comparator low cycle fatigue origin

Figure 9 illustrates the dislocations observed in a primary α lath (grain 5) beneath the origin of a low cycle fatigue test specimen not subjected to hot salt stress corrosion cracking, in similar testing conditions. A low magnification view of the TEM foil is provided in Figure 3. A high density of dislocations can be observed for $\mathbf{g}_{0\bar{1}11}$, in common with the low cycle fatigue propagation region (grain 4) already examined. The c-axis of grain 5 is inclined at $\sim 80\,^{\circ}$ to the fatigue loading axis and therefore grain 5 can be directly compared with grains 1 and 2; see Table 1. The observation of a higher dislocation density in the low cycle fatigue crack growth region is consistent with those observed in a conventional low cycle fatigue origin, and quite distinct from those in the hot salt stress corrosion crack origin region. Thus, an effect of crack length can be excluded as an explanation for the observations made.

[Figure 9 about here.]

4. Discussion

4.1. Comparability of FIB and electropolished TEM foils

Several studies have discussed the surface damage associated with FIB prepared thin foils. When the gallium beam impinges on the sample surface, Ga^{+} ions are implanted in the lattice of the target material. This can lead to local compositional variations, as well as amorphisation of the outer layers of the foil [37]. Gallium penetration depth increases with beam energy (accelerating voltage). More Ga^{+} interstitials would therefore be expected after bombardment at 30 keV compared to 5 keV. These interstitial Ga^{+} ions impose strain on the crystal lattice and hence generate strain contrast in the TEM. Kiener et al. [38] reported that after milling at 30 keV, it was not possible to distinguish individual pre-existing dislocations from the contrast associated with point defects, in the form of Ga^{+} interstitials. However, FIB induced damage can be controlled by reducing the beam energy. Although Kiener et al. still observed some surface damage after irradiation at 5 keV, all pre-existing defects remained

visible. In the present study, final milling at 28 pA and 2 keV was undertaken in an attempt to remove damaged outer layers, whilst minimising further damage.

[Figure 10 about here.]

Figure 10 demonstrates two different imaging conditions for: 1. a primary alpha lath within a FIB prepared foil, and 2. a primary alpha lath within an electropolished foil. Both samples were prepared from as-received material that had undergone no further mechanical deformation since the forging process. For invisibility conditions of $\mathbf{g}_{0002}$, both samples show a low density of linear dislocation segments, which extend across the width of grain. For both preparation techniques the dislocations are also distributed throughout the length of the primary alpha. For an alternative contrast condition of $\mathbf{g}_{0\bar{1}11}$, the dislocation density and distribution is again comparable for the grains in either sample, as is the general appearance of the dislocation segments. Evidence of FIB damage can be seen at both imaging conditions, but is more severe for $\mathbf{g}_{0\bar{1}11}$. The supposed FIB damage can be observed as the speckled contrast throughout the alpha lath, that is likely to be associated with strain accumulation caused by Ga^+ ions implanted during milling. As a result, the dislocations within the FIB foil are slightly less distinctive than those in the electropolished foil. However, the dislocation contrast in the FIB foil remains adequate, so it is possible to differentiate between the dislocations and the FIB damage. It is hence concluded that preparation using FIB milling has not effected the ability to analyse dislocations within α titanium laths.

4.2. Facet formation

Over the past few years, various research groups have raised questions concerning the validity of the common association of planar facet features with a brittle, cleavage, fracture mechanism. Pilchak et al. found that thousands of fatigue load cycles could contribute to the formation of a single facet, providing evidence to contradict the cleavage facet formation theory [40]. Bridier et al. discuss observations of both basal and prismatic slip bands, and suggest fatigue

cracks to have formed from these slip planes [41]. Additionally, Bantounas et al. found evidence suggesting facets on a high-cycle fatigue fracture surface to be associated with basal slip [42]. Figure 4 demonstrated pole figures achieved from direct indexing of facets in the hydrogen embrittled origin region. These pole figures suggested the plane of fracture to be a high index plane, such as $(10\bar{1}7)$ or $(10\bar{1}8)$, which are known hydrogen habit planes. The facets in question contain structure, and are certainly not featureless, thus it is suggested that the formation of these low ΔK features arises *via* a slip induced mechanism, perhaps on one of the high index planes stated above.

Figure 11 demonstrates a representative overview of the general fractography observed at a crack length of 600 µm (grain 4). Both secondary cracking, (a) and (b), and striated growth, (c) and (d), are plastic processes, indicating that the material at this crack length has undergone significant plasticity prior to crack propagation. Not only do the secondary cracks appear to be held open, but the fine ligaments of material between individual striations are observed to have torn apart, 11(d), which is a further indication of significant plasticity. Contrastingly, the material within the hydrogen embrittled region is largely facetted and has a macroscopically brittle appearance (grains 1-3); refer to Chapman et al., Figure 4 [29].

[Figure 11 about here.]

4.3. Grain orientation

It has been well documented that under fatigue loading conditions, grains will deform *via* particular slip systems depending on their orientation. For single crystals, a specific slip system is favoured depending on, 1: the critical resolved shear stress (CRSS) necessary to initiate slip on the given system (also dependent on temperature), and 2: the Schmid factor, which is a function of grain orientation with respect to the loading axis. It is more complicated for polycrystals, where the orientation of neighbouring grains, as well as the orientation of adjacent grain boundaries, can affect slip mechanisms. Bantounas

et al. attempted to predict the active slip system of a given grain by introducing a term defined as a normalised Schmid factor, m', given by

$$m' = m \cdot \left(\tau_{min}/\tau_{\langle uvtw\rangle\{hkil\}}\right) \tag{1}$$

where the $\left(\tau_{min}/\tau_{\langle uvtw\rangle\{hkil\}}\right)$ component is the ratio of the minimum CRSS to activate any slip system *vs.* the CRSS of a particular slip system [43]. According to this rationale, it was expected that grains 1 and 2 would undergo $\langle a\rangle$ prismatic slip, and grain 3 $\langle a\rangle$ basal slip. Instead, we have suggested above that grains 1 and 2 underwent $\langle a\rangle$ basal slip and grain 3 $\langle a\rangle$ 1$^{\text{st}}$ order pyramidal slip. It is suggested that this lack of conformity indicates a change in deformation mechanism, that may be attributed to solute hydrogen.

Since it is possible to disregard any effects relating to crack length, grains 1, 2 and 5 can be directly compared (hard orientation), with the same for grains 3 and 4 (soft orientation); Table 1. Although in each case the grains are only slightly misorientated, their dislocation density and distribution is very different. Considering their similar alignment to the loading axis, this disparity cannot be explained as a consequence of grain orientation. Instead, solute hydrogen at or near the crack tip during the fracture of grain 3 is suggested to affect the plastic behaviour of the grain. This idea is reiterated, since grains 1 and 2 have a hard, rather than soft, orientation, but still demonstrate a similar dislocation distribution and density to grain 3.

4.4. Solute hydrogen diffusion

This study has demonstrated a clear change in micro-deformation mechanisms likely to be associated with solute hydrogen, and the consequent embrittlement *via* hydrogen enhanced localised plasticity. In this particular case, a naturally occurring hydrogen embrittled fatigue crack origin has been investigated. Reactions leading to the production of hydrogen and its consequent adsorption are given in the accompanying paper [29], where it is explained there is a finite supply of hydrogen. It is also considered that only relatively low concentrations of hydrogen are involved in the mechanism, which may explain the lack

of observed hydride phases. Bache et al. suggested that hydrogen may have the most significant effect on dislocation behaviour when present in lower concentrations [44]. Of course, hydrogen diffusivity is proportional to temperature. The rapid diffusion of hydrogen in the beta phase at elevated temperatures is the property that makes the HELP mechanism conceivable. For the bulk specimens discussed in this study, the test temperature was 450 °C, which is sufficiently high to elevate hydrogen mobility. Another observation linked to test temperature was the inclined dislocation segments in grains 1 and 2. These segments were observed to have a different Burgers vector to the majority of the linear dislocation array. When two edge dislocations intersect, one dislocation cuts through the glide plane of another, creating a jog. A jog will form in the glide plane of a mobile dislocation when its dislocation line vector is not parallel to the Burgers vector of the interacting dislocation. Hence, the jog will lie in the plane of the intersecting dislocation, and in this case, will have a different Burgers vector to other dislocations gliding in the original slip plane before intersection. It is suggested that the short inclined dislocation segments observed in grains 1 are 2 are formed as jogs. Motion of these jogs is a diffusion controlled process only possible at elevated temperatures, such as those experienced here. Interestingly, the inclination of these jogs is $\sim 120\,^{\circ}$ to the basal trace, which is also the approximate angle between both the $\{1\bar{1}01\}$ and $\{\bar{1}\bar{1}22\}$ pyramidal planes with the basal plane. Therefore, it is suggested that under high temperature, some edge dislocations moved out of their glide plane by climb on the pyramidal $\{1\bar{1}01\}\langle 11\bar{2}3\rangle$ or $\{\bar{1}\bar{1}22\}\langle 11\bar{2}3\rangle$ slip systems.

4.5. A rationale for lower dislocation density with solute hydrogen

It is well documented that hydrogen increases the mobility of dislocations [20, 31, 32, 44, 33]. Shih et al. explain that hydrogen enhances plasticity in the vicinity of a crack tip (HELP), altering the local deformation mechanism. Since localised micro-fracture could then occur at stresses below the macroscopic yield stress, it can be considered a locally brittle material response, which may explain the brittle faceted appearance at the hydrogen origin [20].

The Orowan equation describes the relationship between strain rate $\dot{\epsilon}$, dislocation density ρ_m, average velocity $\bar{v}$ and magnitude of the Burgers vector b of the mobile dislocations [45].

$$\dot{\epsilon} = b\rho_m\bar{v} \tag{2}$$

It has previously been discussed that grains 1-3 have a considerably lower dislocation density than grains 4 and 5. This has been attributed to solute hydrogen presence ahead of the fatigue crack origin. This observation can be rationalised using the Orowan equation and the effect of hydrogen. If hydrogen enhances dislocation mobility, raising the dislocation velocity, then at a given strain rate in the crack tip plastic zone, this implies a reduction in the mobile dislocation density. Therefore, with the hydrogen enhancing the mobility of the dislocations, it follows that fewer dislocations should be observed. It is understood that hydrogen enters the lattice at elastic singularities, an example of which is the material immediately ahead of the advancing crack. As the hydrogen concentration is highest at regions such as this, plasticity is constrained locally at the crack tip.

For grains 4 and 5, the opposite is observed. Without hydrogen in solution, dislocations are less mobile. Hence, for the same strain rate, many more dislocations will be observed, resulting in more dislocation interactions. The increased density meant that more dislocation interactions occurred, making jogs. As jogs effectively increase the length of the dislocation line, this hardens the material, as well as further impeding their motion [46]; the more dislocations cutting through the "forest" of dislocations, the harder the material becomes. This is commonly referred to as forest hardening, consistent with observations from grain 4. It is generally considered that screw dislocations control deformation in the α phase [30, 47], since edge segments are believed to move at least 100 times faster [48]. It has also been suggested that solute hydrogen can "increase the propensity for edge character dislocations" [33], explaining why the frequency of occurrence of edge dislocations may have been higher in the hydrogen embrittled grains analysed in this study. It also follows that since edge

dislocations are considered to be highly mobile [49], their increased presence in the hydrogen embrittled grains is consistent with the HELP mechanism and the Orowan equation.

4.6. Consistency of the HELP mechanism with the observation of macroscopic hardening

The HELP concept was first introduced by Beachem [21], and has since been the subject of extensive TEM investigations by Birnbaum, Shih, Sofronis, Robertson and coworkers. Shih et al., using *in situ* straining in the TEM, report that the velocity of dislocations near a crack tip in a thin foil is enhanced when hydrogen is added to an environmental cell under constant stress [20]. Birnbaum and Robertson have since proposed that hydrogen shielding of dislocation-dislocation interactions would explain their observation of enhanced dislocation mobility [31, 33]. They believe that this elastic shielding allows dislocations to move at lower applied stress levels in the presence of hydrogen, resulting in localised flow softening at a crack tip.

In contrast, other work [50, 51, 52] has found that hydrogen in solution increases the macroscopic flow stress, implying solute hardening. The solubility of H in Ti at room temperature is approximately 0.1 at.% ($\sim$ 20 ppmw) [53]. These studies suggest that this solute hardening is due to a dislocation pinning effect, although it should be noted that the hydrogen atom is small compared to the interstitial site, which is a drawback to this rationale. Beachem, observing hydrogen-assisted cracking and an associated reduction in fracture toughness, suggested that hydrogen unlocks dislocations, rather than pinning them [21].

Therefore it remains to rationalise how hydrogen, *e.g.* at a hot salt stress corrosion crack tip, can reduce toughness, enhance dislocation mobility and yet provide macroscopic hardening. A primary difference between a crack tip or thin foil and the bulk is the availability of a free surface. This could allow gliding dislocations to escape. Therefore, if appealing to the Orowan equation, the HELP mechanism gives rise higher glide velocities, and so to a lower dislocation density for a given strain rate, then in the bulk this would then result in larger

glide lengths and more opportunity for dislocation tangling or forest hardening. Whereas, in the presence of a free surface, this straining can occur without a gradual rise in dislocation density.

In addition, these observations are consistent with the reduction of K_{Ic} with hydrogen content - hydrogen embrittlement is a consequence of enhanced plasticity and dislocation motion at the crack tip, rather than requiring the alternative that decohesion (the formation of free surface) becomes easy even at the very low H contents in (solid) solution that pertain in the present case, as proposed by Lynch [54].

Thus, the present observation of a lower dislocation density below a stress corrosion crack than in low cycle fatigue is consistent with both the observations of Shih and the HELP mechanism, and the observation of macroscopic flow hardening and reduced fracture toughness.

4.7. Critical diffusion length

The significant difference in dislocation density, and its association with solute hydrogen, has been discussed in detail. This was attributed to the ability of hydrogen to enhance dislocation motion. It is also observed, that for hydrogen embrittled grains, dislocations appear to be restricted to within a 3 µm depth beneath the fracture surface. Whereas for grain 4 (crack propagation), the high density of dislocations continue throughout the length of the primary alpha lath, which intersects the fracture surface at $\sim 90\,^{\circ}$. This observation can be explained by considering the competitive processes of hydrogen charging and hydrogen diffusion. The reader is referred to the accompanying paper by Chapman et al. [29], for a detailed explanation of these reactions, but the important points are summarised here.

When the rate of hydrogen charging exceeds the rate of hydrogen diffusion, the local hydrogen concentration immediately in front of the crack is sufficiently high to embrittle the material locally, via the HELP mechanism. The grain experiences highly localised enhanced plastic strain and undergoes deformation in the vicinity of the crack tip, leading to crack advance.

It is proposed that the localised nature of the deformation causes HELP to act over only the portion of the grain closest to the newly created fracture surface. It follows that the lower region of the primary alpha lath will not experience enhanced plasticity before the crack front advances. Therefore, assuming constant hydrogen charging and diffusion rates at a given temperature, it is postulated that there is a critical diffusion distance, beyond which charging is insufficient to cause embrittlement. Hence, because HELP is not active beyond this critical diffusion length, L_D, hydrogen enhanced fracture mechanisms are constrained to the uppermost material, estimated at 3 µm for grains 1-3. It should also be noted, that when L_D is of the same order of magnitude as the crack growth increment per fatigue cycle, there is no possibility for hydrogen accumulation over multiple cycles. Recent work by Gaddam et al., discusses this area in more detail [55].

Alternatively, turning to the AIDE hypothesis, we first consider that at 450 °C, then the hydrogen diffusion rate and solubility are both likely high enough for diffusion to a 3µm depth to occur, in contrast to the AIDE situation pertaining at ambient temperatures and high crack growth rates considered by Lynch [54, 23]. As previously noted, there is also the possibility of the β phase acting as a fast diffusion path [28]. But, as has been more recently noted by Lynch [56], it remains possible that dislocation nucleation from hydrogen at the surface might then result in propagation into the depth of the material, in a HELP-like fashion. However, in our view the change in dislocation morphology (particularly those travelling in ribbons in Figure. 7) suggests that rather more is occurring than simply hydrogen-stimulated dislocation emission.

5. Conclusions

The dislocation mechanisms underlying a naturally initiated hot salt stress corrosion crack have been elucidated and compared to those observed in conventional low cycle fatigue. The following conclusions can be drawn.

1. Hydrogen embrittled grains do not appear to conform to the predictions

made by the normalised Schmid factor method, as proposed by Bantounas et al [43].

2. It is proposed that hydrogen in the vicinity of the crack tip modifies dislocation behaviour (which could be through the AIDE or HELP mechanisms).
3. Irrespective of the grain orientation, the dislocation density is consistently, and significantly, lower in hydrogen embrittled grains compared to those from the fatigue crack propagation region and LCF origin.
4. The effect of crack length is excluded as a contributing factor to the increased dislocation density observed in the LCF propagation region.
5. The Orowan equation is used to explain the reduction in dislocation density seen within hydrogen embrittled grains, by considering the elevated dislocation mobility attributed to the onset of HELP at the crack tip.
6. A rationale for the observed flow softening in thin foils *vs.* that of macroscopic hardening in bulk specimens is proposed.
7. A term defined as the critical diffusion length is introduced. It is suggested that the competitive reaction between hydrogen charging and hydrogen diffusion determines the maximum depth beneath the fracture surface that is affected by solute hydrogen (with the HELP mechanism in view).

Acknowledgements

The authors wish to acknowledge support from Rolls-Royce plc throughout this work. We would also like to thank the numerous people involved who are based at Rolls-Royce Derby, Bristol and Dahlewitz. The authors would also like to acknowledge very useful discussions with Prof. Ian Jones. Finally, we are grateful for funding from the EPSRC; grants EP/H004882/1 and EP/K034332/1, as well as a DTA CASE conversion EP/J500239/1 for T.P.C.

References

[1] R. Boyer, Titanium for aerospace: Rationale and applications, Advanced Performance Materials 2 (1995) 349–68.

[2] R. Boyer, An overview of titanium in the aerospace industry, Materials Science and Engineering A A213 (1996) 103–14.

[3] J. Williams, E. J. Starke, Progress in structural materials for aerospace systems, Acta Materialia 51 (2003) 5775–99.

[4] G. Crook, M. Horlor (Eds.), Rolls-Royce - The jet engine, 1996.

[5] G. Lütjering, J. Williams, Titanium, Springer Science, 2003.

[6] M. Blackburn, J. Williams, Metallurgical aspects of the stress corrosion cracking of titanium alloys, in: Proceedings of Conference on Fundamental Aspects of Stress Corrosion Cracking, 1969.

[7] R. Ondrejcin, Chlorine gas and fluoride ion in hot-salt stress corrosion cracking of titanium-aluminium alloys, NASA DP-1179 (1969).

[8] V. Petersen, H. Bomberger, The mechanism of salt attack on titanium alloys, Stress Corrosion Cracking of Titanium: ASTM Special Technical Publication 397 (1966) 80–94.

[9] S. Rideout, M. Louthan Jr., C. Selby, Basic mechanisms of stress-corrosion cracking of titanium, Stress Corrosion Cracking of Titanium: ASTM Special Technical Publication 397 (1966) 137–51.

[10] H. Logan, M. McBee, C. Bechtoldt, B. Sanderson, G. Ugiansky, Chemical and physical mechanisms of salt stress-corrosion cracking in the titanium 8-1-1 alloy, Stress Corrosion Cracking of Titanium: ASTM Special Technical Publication 397 (1966) 215–29.

[11] J. Myers, J. Hall, Hot salt stress-corrosion cracking of titanium alloys: An improved model for the mechanism, Corrosion - NACE 33 (1977) 252–7.

[12] M. Garfinkle, An electrochemical model for hot-salt stress-corrosion of titanium alloys, Metallurgical Transactions 4 (1973) 1677–86.

[13] M. Pustode, V. Raja, N. Paulose, The stress-corrosion cracking susceptibility of near-α titanium alloy IMI834 in presence of hot salt, Corrosion Science 82 (2014) 181–96.

[14] A. Pilchak, A. Young, J. Williams, Stress corrosion cracking crystallography of Ti-8Al-1Mo-1V, Corrosion Science 52 (2010) 3287–96.

[15] B. F. Brown, Stress Corrosion Cracking in High Strength Steels and in Titanium and aluminium alloys, Naval Research Laboratory, 1972.

[16] E. Tal-Gutelmacher, D. Eliezer, Hydrogen-assisted degradation of titanium based alloys, Materials Transactions 45 (2004) 1594–600.

[17] T. MacKay, Effect of stress on microsegregation of hydrogen at elevated temperatures in titanium and Ti-8Al-1Mo-1V, Metallurgical Transactions 2 (1971) 2299–302.

[18] H. Nelson, Aqueous chloride stress corrosion cracking of titanium - a comparison with environmental hydrogen embrittlement, NASA TM X-62314 (1973).

[19] H. Nelson, A film-rupture model of hydrogen-induced, slow crack growth in acicular alpha-beta titanium, Metallurgical Transactions A 7A (1976) 621–7.

[20] D. Shih, I. Robertson, H. Birnbaum, Hydrogen embrittlement of α titanium: *in situ* TEM studies, Acta Metallurgica 36 (1988) 111–24.

[21] C. Beachem, A new model for hydrogen-assisted cracking (hydrogen "embrittlement"), Metallurgical Transactions 3 (1972) 437–51.

[22] I.M. Robertson, P. Sofronis, A. Nagao, M.L. Martin, S. Wang, D.W. Gross, K.E. Nygren, Hydrogen embrittlement understood, Metallurgical and Materials Transactions B 46B (2015) 1085–103.

[23] S.P. Lynch, Hydrogen embrittlement (HE) phenomena and mechanisms, Corrosion Reviews 30 (2012) 105–23.

[24] S.P. Lynch, Mechanisms and Kinetics of Environmentally Assisted Cracking: Current Status, Issues, and Suggestions for Further Work, Metallurgical and Materials Transactions A 44A (2013) 1209–29.

[25] S.P. Lynch, A fractographic study of gaseous hydrogen embrittlement and liquid-metal embrittlement in a tempered-martensitic steel, Acta Metallurgica 32 (1984) 79–90.

[26] E. Tal-Gutelmacher, D. Eliezer, The hydrogen embrittlement of titanium-based alloys, Journal of Materials Overview (2005) 46–9.

[27] H. Nelson, D. Williams, J. Stein, Environmental hydrogen embrittlement of an α-β titanium alloy: Effect of microstructure, Metallurgical Transactions 3 (1972) 469–75.

[28] P. Pao, J. O'Neal, Hydrogen enhanced fatigue crack growth in Ti-6242s, Journal of Nuclear Materials 122/123 (1984) 1587–91.

[29] T. Chapman, R. Chater, E. Saunder, A. Walker, T. Lindley, D. Dye, Environmentally assisted fatigue crack nucleation in Ti-6Al-2Sn-4Zr-6Mo, Corrosion Science 96 (2015) 87–101.

[30] F. Mignot, V. Doquet, C. Sarrazin-Baudoux, Contributions of internal hydrogen and room-temperature creep to the abnormal fatigue cracking of Ti6246 at high K_{max}, Materials Science and Engineering A 380 (2004) 308–19.

[31] P. Birnbaum, H.K. Sofronis, Hydrogen-enhanced localized plasticity - a mechanism for hydrogen-related fracture, Materials Science and Engineering A 176 (1994) 191–202.

[32] P. Ferreira, I. Robertson, H. Birnbaum, Hydrogen effects on the interaction between dislocations, Acta Materialia 46 (1998) 1749–57.

[33] I. Robertson, The effect of hydrogen on dislocation dynamics, Engineering Fracture Mechanics 65 (2001) 649–73.

[34] V. Sinha, M. Mills, J. Williams, Crystallography of fracture facets in a near-α titanium alloy, Metallurgical and Materials Transactions A 37 (2006) 2015–26.

[35] V. Sinha, M. Mills, J. Williams, Determination of the crystallographic orientation of dwell-fatigue fracture facets in Ti-6242 alloy, Journal of Materials Science 42 (2007) 8334–41.

[36] G. Themelis, S. Chikwembani, J. Weertman, Determination of the orientation of Cu-Bi grain boundary facets using a photogrammetric technique, Materials Characterization 24 (1990) 27–40.

[37] L. Giannuzzi, F. Stevie, A review of focused ion beam milling techniques for TEM specimen preparation, Micron 30 (1999) 197–204.

[38] D. Kiener, C. Motz, M. Rester, M. Jenko, G. Dehm, FIB damage of Cu and possible consequences for minitarized mechanical tests, Materials Science and Engineering A 459 (2007) 262–72.

[39] N. Paton, R. Spurling, Hydride habit planes in titanium-aluminium alloys, Metallurgical Transactions A 7 (1976) 1769–174.

[40] A. Pilchak, A. Bhattacharjee, A. Rosenberger, J. WIlliams, Low ΔK faceted growth in titanium alloys, International Journal of Fatigue 31 (2009) 989–94.

[41] F. Bridier, P. Villechaise, J. Mendez, Slip and fatigue crack formation processes in an α/β titanium alloy in relation to crystallographic texture on different scales, Acta Materialia 56 (2008) 3951–62.

[42] I. Bantounas, D. Dye, T. Lindley, The role of microtexture on the faceted fracture morphology in Ti-6Al-4V subjected to high-cycle fatigue, Acta Materialia 58 (2010) 3908–18.

[43] I. Bantounas, D. Dye, T. Lindley, The effect of grain orientation on fracture morphology during high-cycle fatigue of Ti-6Al-4V, Acta Materialia 57 (2009) 3584–95.

[44] M. Bache, W. Evans, H. Davies, Electron back scattered diffraction (EBSD) analysis of quais-cleavage and hydrogen induced fractures under cyclic and dwell loading in titanium alloys, Journal of Materials Science 32 (1997) 3435–42.

[45] D. Hull, D. Bacon, Introduction to Dislocations, Butterworth-Heinemann, 2001.

[46] M. Sangid, The physics of fatigue crack initiation, International Journal of Fatigue 57 (2013) 58–72.

[47] P. Castany, F. Pettinari-Sturmel, J. Douin, A. Coujou, In situ transmission electron microscopy deformation of the titanium alloy Ti-6Al-4V: Interface behaviour, Materials Science and Engineering A 483-484 (2008) 719–22.

[48] P. Castany, F. Pettinari-Sturmel, J. Crestou, J. Douin, A. Coujou, Experimental study of dislocation mobility in a Ti-6Al-4V alloy, Acta Materialia 55 (2007) 6284–91.

[49] S. Naka, A. Lasalmonie, P. Costa, L. Kubin, The low-temperature plastic defomration of α-titanium and the core structure of a-type screw dislocations, Philosophical Magazine A 57 (1988) 717–40.

[50] H. Matsui, H. Kimura, S. Moriya, The effect of hydrogen on the mechanical properties of high purity iron I. Softening and hardening of high purity iron by hydrogen charing during tensile deformation, Materials Science and Engineering 40 (1979) 207–16.

[51] W. Xie, X. Liu, W. Chen, H. Zhang, Hydrogen hardening effect in heavily deformed single crystal α-Fe, Computational Materials Science 50 (2011) 3397–402.

[52] F. Beck, Effect of hydrogen on the mechanical properties of titanium and its alloys, Technical Report CR-134796, NASA, 1975.

[53] H. Conrad, Effect of interstitial solutes on the strength and ductility of titanium, Progress in Materials Science 26 (1981) 123–403.

[54] S. Lynch, Progress towards understanding mechanisms of hydrogen embrittlement and stress corrosion cracking, in: Corrosion-NACE, Nashville, TN, 2007.

[55] R. Gaddam, M. Perderson, R. Hörnqvist, M.-L. Antti, Fatigue crack growth behaviour of forged Ti-6Al-4V in gaseous hydrogen, Corrosion Science 78 (2014) 378–83.

[56] S.P. Lynch, Metallographic and fractographic techniques for characterising and understanding hydrogen-assisted cracking of metals. In R.P. Gangloff and B.P. Somerday (eds.), Gaseous hydrogen embrittlement of metals in energy technologies - Volume 1: The problem, its characterisation and effects on particular alloy classes, Cambridge, (2012), 274–346.

List of Figures

1 Bright field (BF) TEM images: (a) Overview of lamellar α/β microstructure, (b) and (c) Primary and secondary alpha laths, (d) Secondary alpha residing between coarse primary alpha laths. 30

2 The hydrogen embrittled zone is demonstrated by the blue semi-elliptical feature at the fatigue crack origin. The locations of the facets for the QTF/EBSD technique, as well as the position of the foils for dislocation contrast analysis, are given. 31

3 Position of the grains of interest within the respective FIB-prepared TEM foils. 32

4 [0001] pole figures obtained from facets within the hydrogen embrittled origin: (a) Facet 1 $\sim$14 $^\circ$ from the basal plane , (b) Facet 2 $\sim$14 $^\circ$ from the basal plane. 33

5 BF dislocation contrast images for grain 1, for diffraction conditions of $\mathbf{g}_{0002}$, $\mathbf{g}_{0\bar{1}1\bar{1}}$ and $\mathbf{g}_{0\bar{1}11}$. The white arrows indicate the direction of the $\mathbf{g}$ vector. 34

6 BF dislocation contrast images for grain 2: (Upper) Stitch of low magnification images for $\mathbf{g}_{0002}$, (Lower) Increased magnification views for $\mathbf{g}_{0002}$ and $\mathbf{g}_{0\bar{1}1\bar{1}}$. The dashed box indicates the area magnified from the stitch in the lower left image. In all cases, the white arrow indicates the direction of the $\mathbf{g}$ vector. 35

7 BF dislocation contrast images for grain 3, for diffraction conditions of $\mathbf{g}_{0002}$, $\mathbf{g}_{\bar{2}110}$ and $\mathbf{g}_{0\bar{1}12}$. The arrows indicate the direction of the $\mathbf{g}$ vector. 36

8 BF dislocation contrast images for grain 4, for diffraction conditions of $\mathbf{g}_{0002}$. The white arrows indicate the direction of the $\mathbf{g}$ vector. 37

9 BF dislocation contrast images for grain 5, for diffraction conditions of $\mathbf{g}_{0\bar{1}11}$. The white arrows indicate the direction of the $\mathbf{g}$ vector. 38

10 BF dislocation contrast images for FIB and electropolished prepared thin foils, for diffraction conditions of $\mathbf{g}_{0002}$ and $\mathbf{g}_{0\bar{1}11}$. The white arrows indicate the direction of the $\mathbf{g}$ vector. 39

11 Secondary electron images taken from the fatigue crack propagation region, all at a crack length of $\sim$600 µm, close to the location from which the foil containing grain 4 was extracted: (a) and (b) secondary cracking, (c) and (d) evidence of underlying microstructure as primary alpha lath structures and torn striations. 40

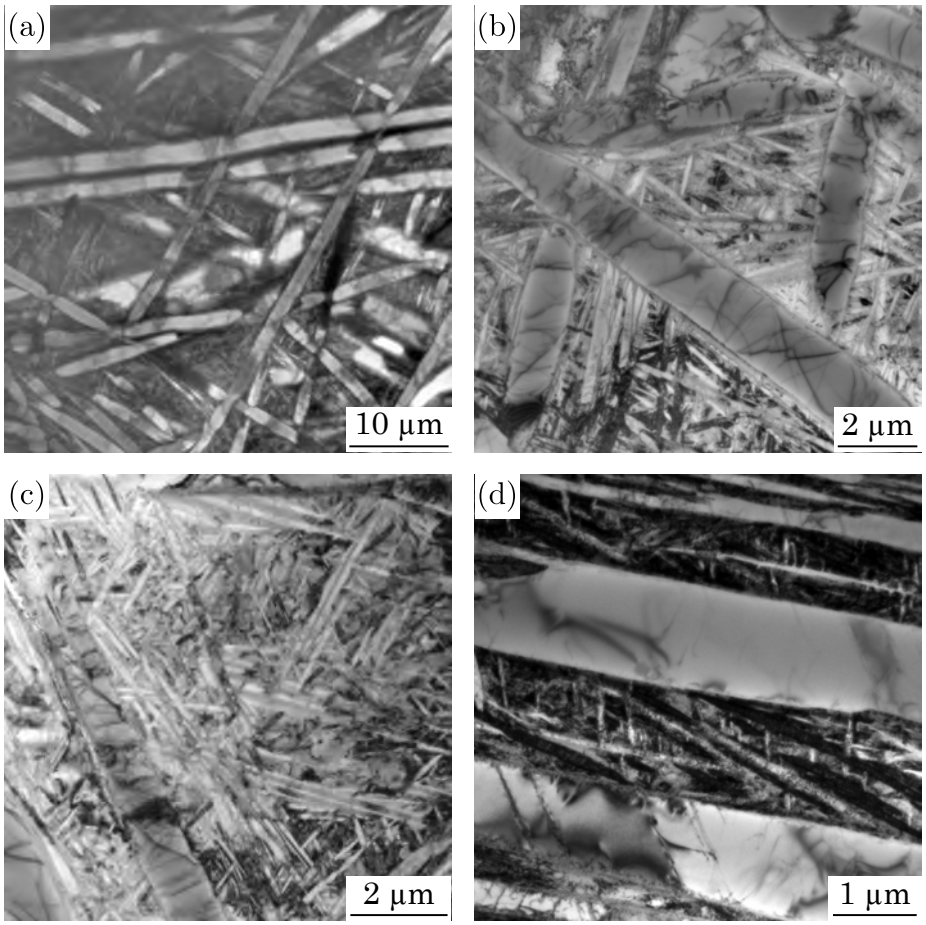

Figure 1: Bright field (BF) TEM images: (a) Overview of lamellar α/β microstructure, (b) and (c) Primary and secondary alpha laths, (d) Secondary alpha residing between coarse primary alpha laths.

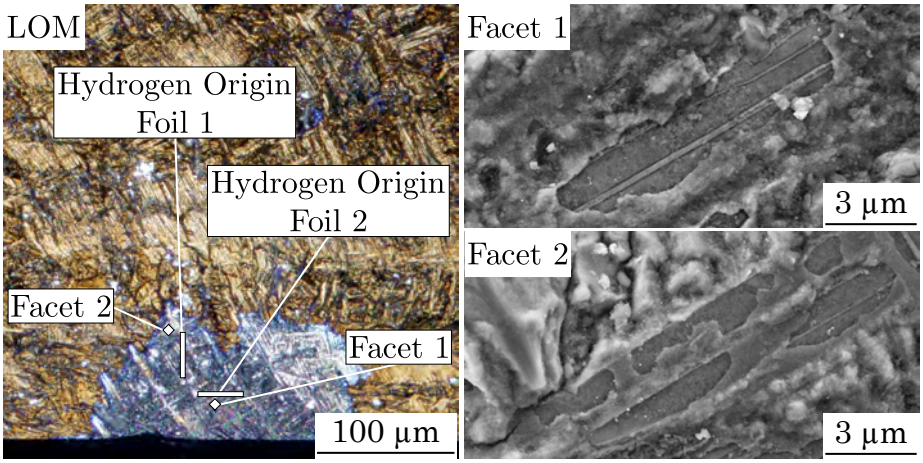

Figure 2: The hydrogen embrittled zone is demonstrated by the blue semi-elliptical feature at the fatigue crack origin. The locations of the facets for the QTF/EBSD technique, as well as the position of the foils for dislocation contrast analysis, are given.

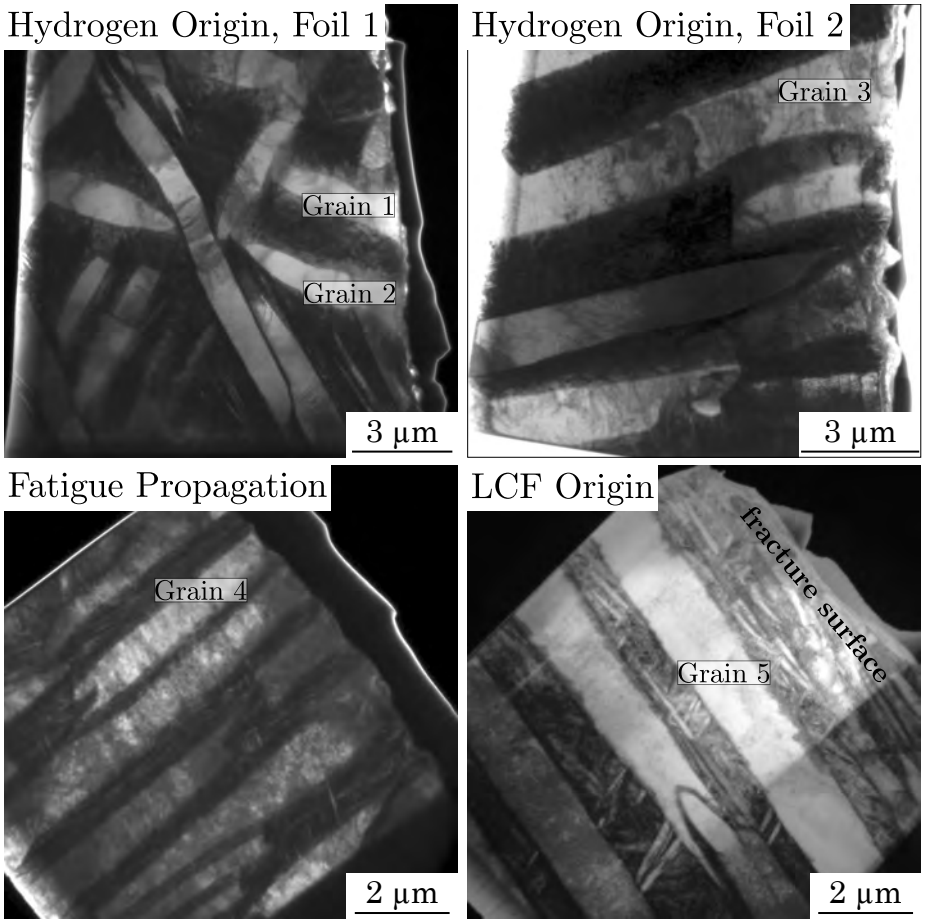

Figure 3: Position of the grains of interest within the respective FIB-prepared TEM foils.

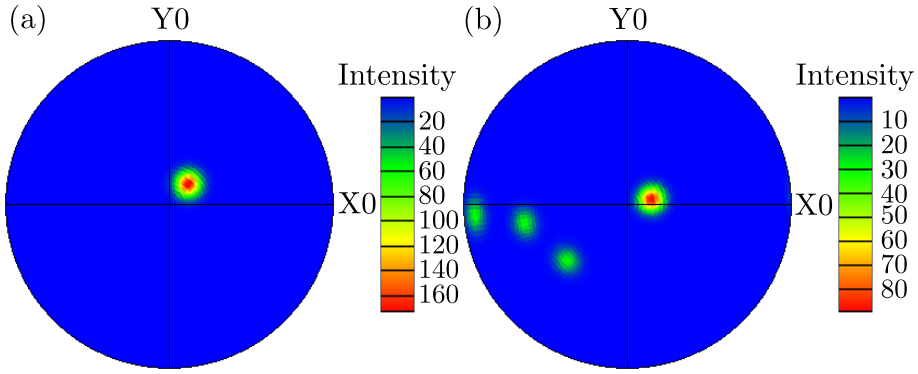

Figure 4: [0001] pole figures obtained from facets within the hydrogen embrittled origin: (a) Facet 1 $\sim 14^\circ$ from the basal plane , (b) Facet 2 $\sim 14^\circ$ from the basal plane.

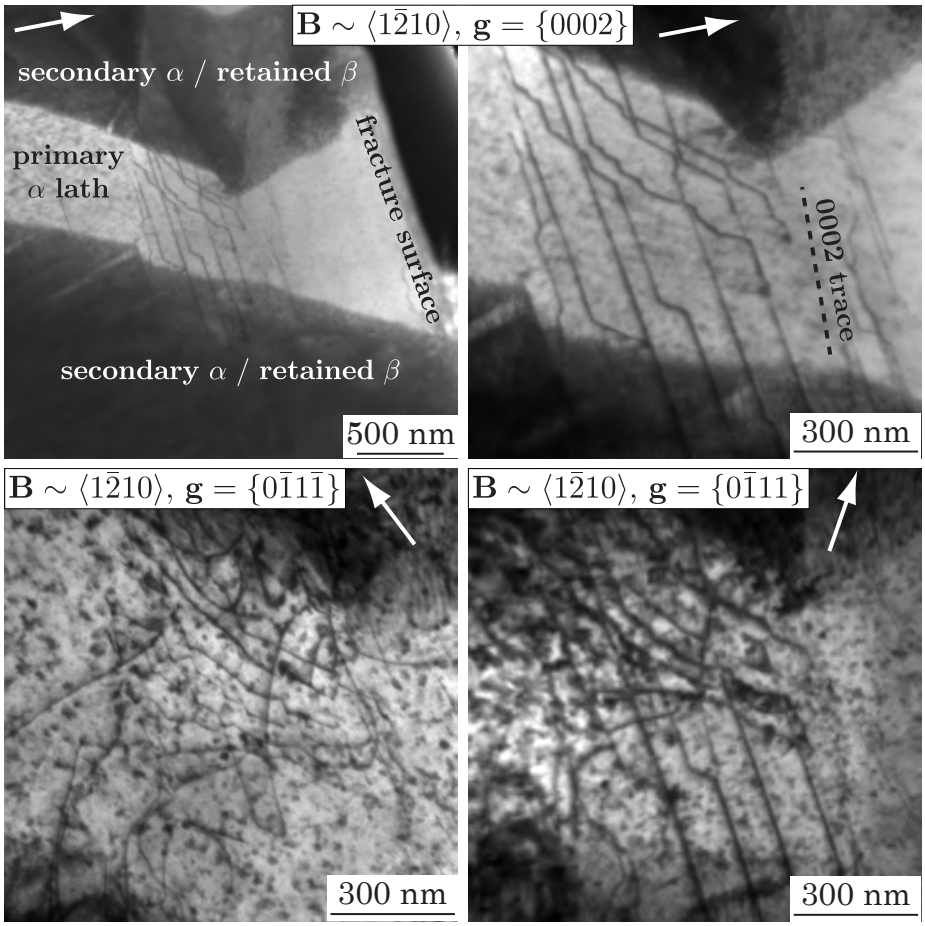

Figure 5: BF dislocation contrast images for grain 1, for diffraction conditions of $\mathbf{g}_{0002}$, $\mathbf{g}_{0\bar{1}1\bar{1}}$ and $\mathbf{g}_{0\bar{1}11}$. The white arrows indicate the direction of the $\mathbf{g}$ vector.

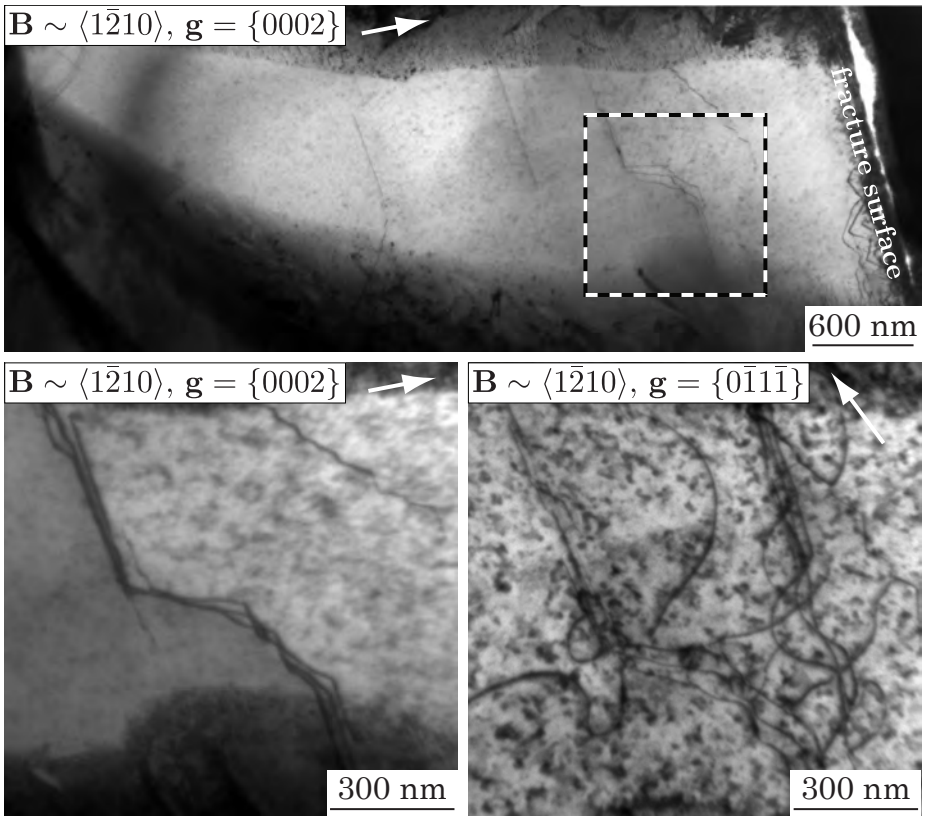

Figure 6: BF dislocation contrast images for grain 2: (Upper) Stitch of low magnification images for $\mathbf{g}_{0002}$, (Lower) Increased magnification views for $\mathbf{g}_{0002}$ and $\mathbf{g}_{0\bar{1}1\bar{1}}$. The dashed box indicates the area magnified from the stitch in the lower left image. In all cases, the white arrow indicates the direction of the $\mathbf{g}$ vector.

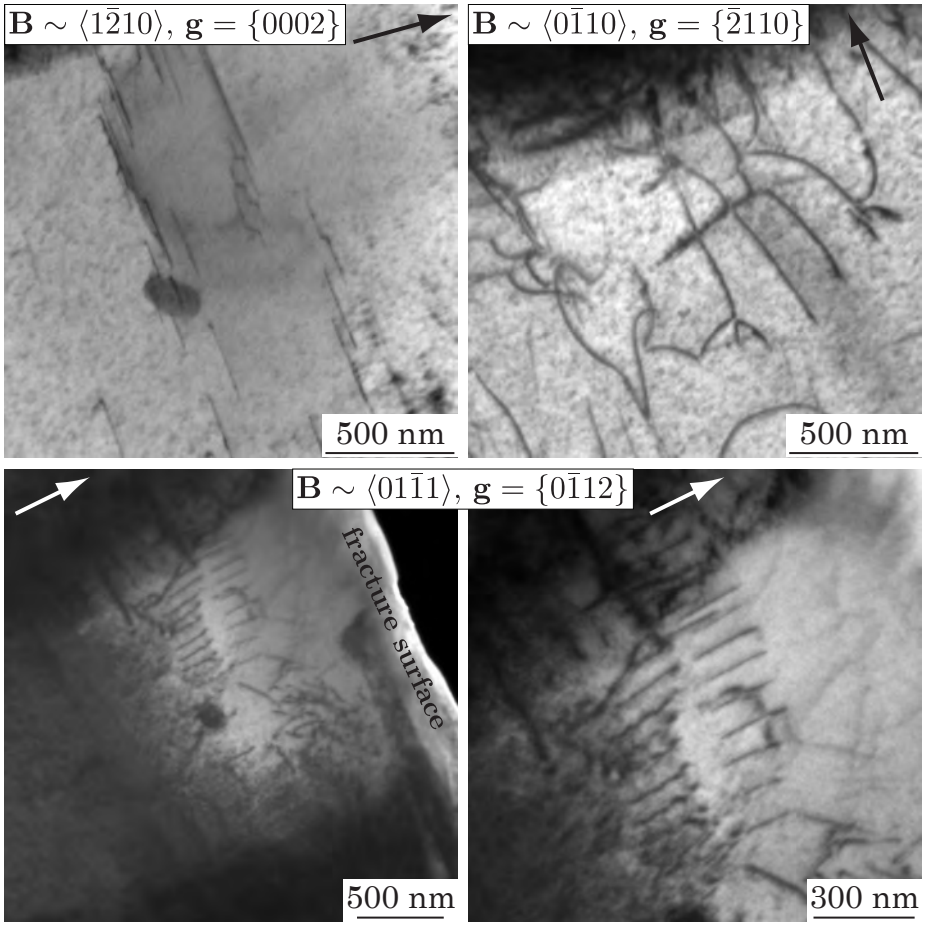

Figure 7: BF dislocation contrast images for grain 3, for diffraction conditions of $\mathbf{g}_{0002}$, $\mathbf{g}_{\bar{2}110}$ and $\mathbf{g}_{0\bar{1}12}$. The arrows indicate the direction of the $\mathbf{g}$ vector.

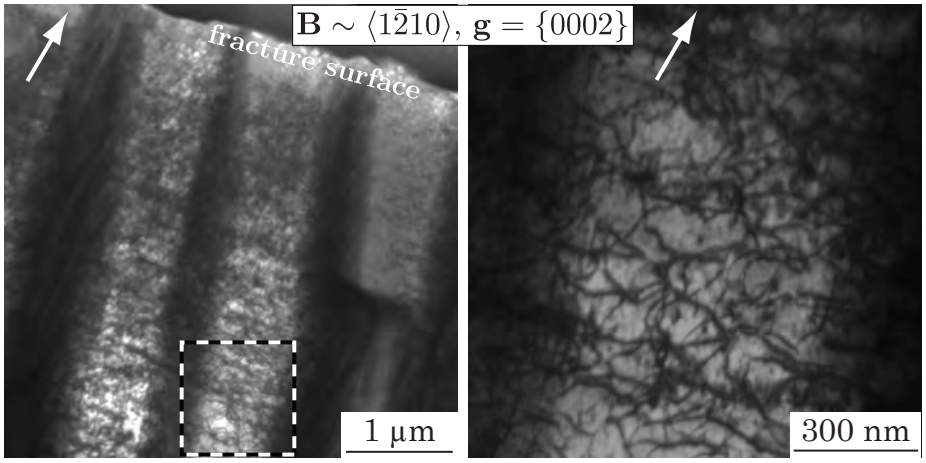

Figure 8: BF dislocation contrast images for grain 4, for diffraction conditions of $\mathbf{g}_{0002}$. The white arrows indicate the direction of the $\mathbf{g}$ vector.

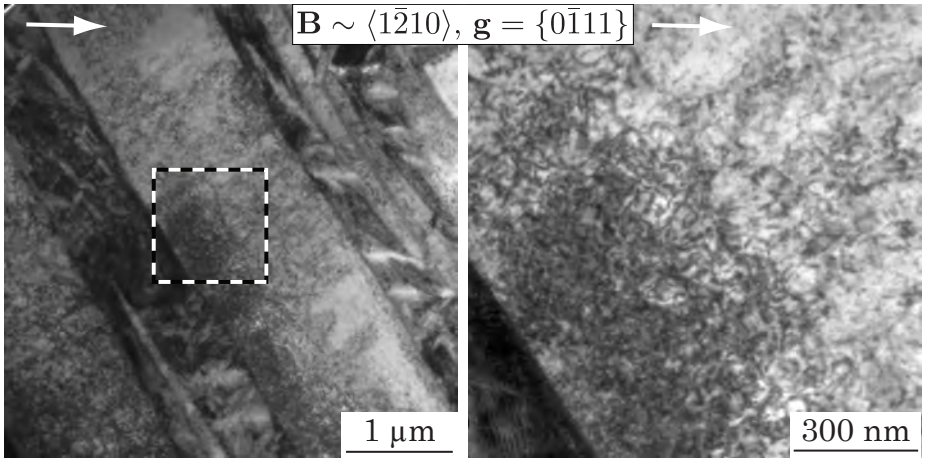

Figure 9: BF dislocation contrast images for grain 5, for diffraction conditions of $\mathbf{g}_{0\bar{1}11}$. The white arrows indicate the direction of the $\mathbf{g}$ vector.

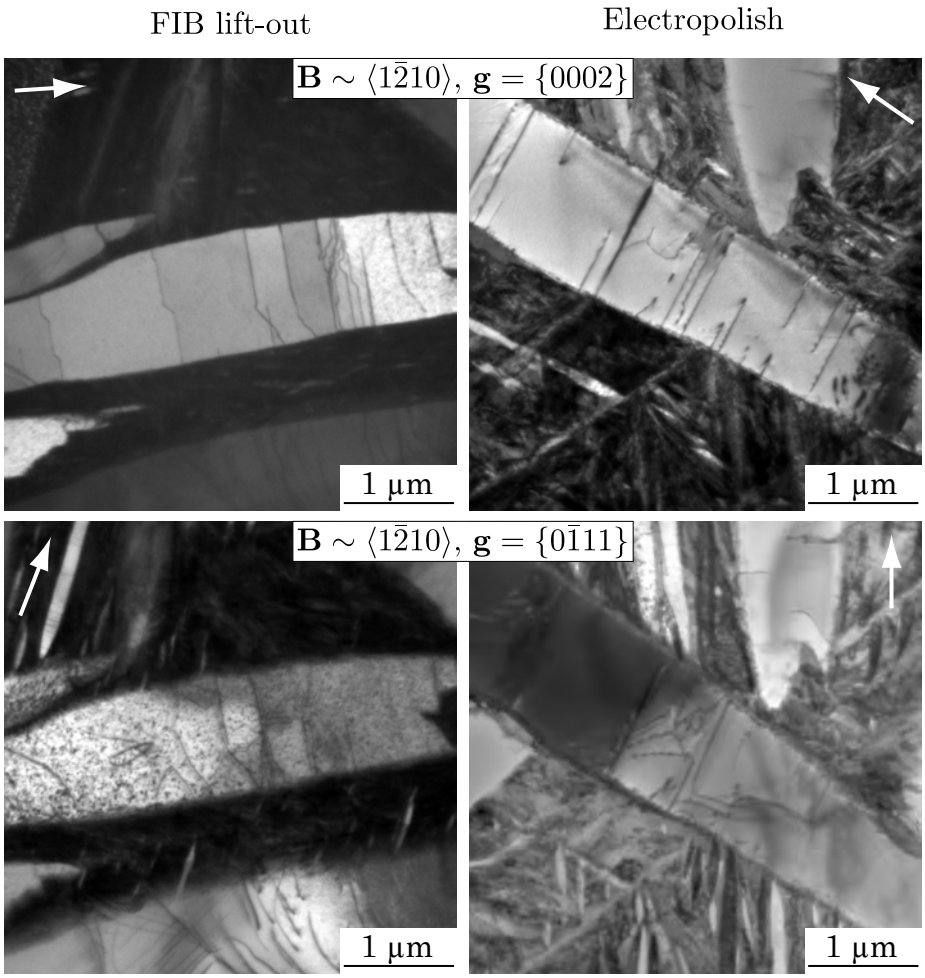

Figure 10: BF dislocation contrast images for FIB and electropolished prepared thin foils, for diffraction conditions of $\mathbf{g}_{0002}$ and $\mathbf{g}_{0\bar{1}11}$. The white arrows indicate the direction of the $\mathbf{g}$ vector.

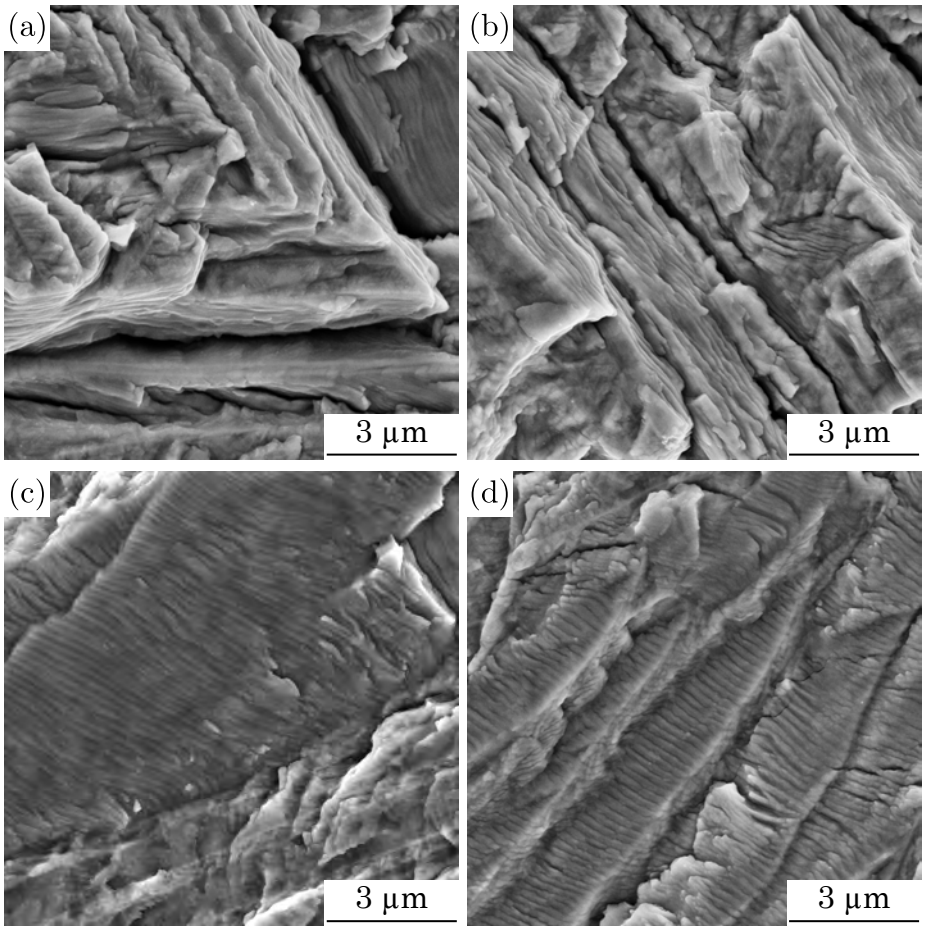

Figure 11: Secondary electron images taken from the fatigue crack propagation region, all at a crack length of ∼600 µm, close to the location from which the foil containing grain 4 was extracted: (a) and (b) secondary cracking, (c) and (d) evidence of underlying microstructure as primary alpha lath structures and torn striations.

List of Tables

1 Location and orientation of grains, where θ is defined as the angle between the loading direction and the c-axis. 42
2 Demonstrating selected invisibility contrast values, where contrast is defined as + and invisibility is defined as 0. 43

Grain ID	Description	θ
1	Hydrogen Embrittled LCF Origin	71 °
2	Hydrogen Embrittled LCF Origin	71 °
3	Hydrogen Embrittled LCF Origin	25 °
4	LCF Crack Propagation	31 °
5	LCF Origin	77 °

Table 1: Location and orientation of grains, where θ is defined as the angle between the loading direction and the c-axis.

Character	Type	**b**	Glide Plane	Invisibility Contrast					
				$\mathbf{g}_{0002}$	$\mathbf{g}_{0\bar{1}1\bar{1}}$	$\mathbf{g}_{0\bar{1}11}$	$\mathbf{g}_{0\bar{1}12}$	$\mathbf{g}_{\bar{2}110}$	$\mathbf{g}_{10\bar{1}0}$
Screw	$\langle a \rangle$	$\frac{1}{3}[\bar{1}\bar{1}20]$	(0001) or $(10\bar{1}0)$ or $(\bar{1}\bar{1}01)$	0	+	+	+	+	+
Screw	$\langle c+a \rangle$	$\frac{1}{3}[1\bar{2}13]$	$(\bar{1}\bar{1}22)$ or $(\bar{1}011)$	+	+	+	+	+	0
Edge	$\langle a \rangle$	$\frac{1}{3}[\bar{1}\bar{1}20]$	(0001)	+	+	+	+	0	0
Edge	$\langle a \rangle$	$\frac{1}{3}[\bar{1}\bar{1}20]$	$(\bar{1}100)$	0	+	+	+	+	+
Edge	$\langle a \rangle$	$\frac{1}{3}[\bar{1}\bar{1}20]$	$(\bar{1}101)$	+	+	0	+	+	+
Edge	$\langle c+a \rangle$	$\frac{1}{3}[1\bar{2}13]$	$(\bar{1}101)$	+	+	0	+	+	+

Table 2: Demonstrating selected invisibility contrast values, where contrast is defined as + and invisibility is defined as 0.